nature communications

Article

https://doi.org/10.1038/s41467-026-71989-6

Structure of a contractile injection system in *Salmonella enterica* subsp. *salamae*

Received: 17 June 2025

Accepted: 2 April 2026

Published online: 16 April 2026

Check for updates

Rooshanie N. Ejaz[1,2], Kristin Funke[3], Claudia S. Kielkopf[1,2], Freddie J. O. Martin[1,2], Marta Šiborová[1,2], Ivo A. Hendriks[2], Nicholas H. Sofos[2,4], Tillmann Pape[2,4], Eva M. Steiner-Rebrova[5], Michael L. Nielsen[1,6], Marc Erhardt[7] & Nicholas M. I. Taylor[1,2]

Extracellular contractile injection systems (eCISs) are phage-derived nanomachines used by bacteria to deliver effectors into target cells. Well-studied examples include the *Photorhabdus asymbiotica* virulence cassettes and the antifeeding prophage from *Serratia entomophila*, which have been engineered for heterologous cargo delivery. Recent genomic analyses identified eCIS gene clusters in the opportunistic human pathogen *Salmonella enterica* subspecies *salamae*, but their structure, function, and biotechnological potential remain unexplored. Here, we report a high-resolution cryo-electron microscopy structure of the *S. enterica* eCIS. Our atomic models reveal a distinctive sheath architecture, an expansive cage-like shell around a central spike, and an associated integral membrane protein. We identify a putative effector encoded within the operon exhibiting mild periplasmic toxicity and provide evidence that the *S. enterica* eCIS deviates from canonical eCISs by interacting with the inner membrane. Guided by these structural features, we uncover, to the best of our knowledge, a previously unannotated cluster of contractile injection systems (CISs). Together, our findings expand the known diversity of CISs' structures and functions, and lay the groundwork for engineering customisable protein delivery platforms.

Extracellular contractile injection systems (eCISs) are macromolecular complexes expressed by bacteria and archaea[1–5]. Evolutionarily derived from the contractile tails of bacteriophages[6–8], they assemble into nanoscale injectors[6], capable of targeted piercing of prokaryotic and eukaryotic cell membranes[5,9,10] to deliver protein payloads. Bacterial cells synthesise eCISs and presumably undergo lysis upon a triggering event[2,11], allowing these systems to leave the cytoplasm and inject effectors across membranes of target cells[12,13]. eCISs have been bioengineered to deliver customised payloads as therapeutics and biopesticides[12,14]. Studying eCIS function and structure in opportunistic human pathogens, such as *Salmonella* species, could provide biomedically relevant insights into non-characterised injection systems.

Canonical eCISs comprise a baseplate, long tail fibres, and a contractile sheath surrounding an inner tube terminating in a cap[1,5,6,9]. The most well-studied of these canonical extracellular systems are the Antifeeding prophage (Afp)[9,15,16] and the *Photorhabdus* virulence

[1]Department of Drug Design and Pharmacology, Faculty of Health and Medical Sciences, University of Copenhagen, Copenhagen, Denmark. [2]Novo Nordisk Foundation Centre for Protein Research, ICMM, Faculty of Health and Medical Sciences, University of Copenhagen, Copenhagen, Denmark. [3]Institute of Biology–Department of Molecular Microbiology, Humboldt-Universität zu Berlin, Berlin, Germany. [4]Core Facility for Integrated Bioimaging, Centre for Core Facilities (CCF), Faculty of Health and Medical Sciences, University of Copenhagen, Copenhagen, Denmark. [5]Biomedical Centre, Department of Experimental Medical Science, Faculty of Medicine, University of Lund, Lund, Sweden. [6]Department of Molecular Biology and Genetics, Aarhus University, Aarhus, Denmark. [7]Institute of Biology–Department of Molecular Microbiology, Humboldt-Universität zu Berlin, 10115 Berlin, Max Planck Unit for the Science of Pathogens, Berlin, Germany. e-mail: nicholas.taylor@sund.ku.dk

cassettes (PVC)[5,12,13]. eCISs share structural features with contractile injection systems (CIS), such as Type VI secretion systems (T6SS), including their outer membrane anchor-deficient subtypes (T6SS$^{ii\text{-}iv}$) and tailocins[6,17]. AlgoCIS, tCIS and CIS^{Sc} from *Algoriphagus machipongonensis*, cyanobacterium *Anabaena* and *Streptomyces coelicolor*, respectively, were structurally characterised to help elucidate their diverse functions[3,4,18]. CISs can be considered interactive protein complexes, allowing trans-kingdom interactions and involvement in bacterial cell cycles. The role of CISs as interaction tools across bacterial species and clades is expanding[2,3,18]. The current canonical mechanism of action on eCIS release remains that they are extracellularly released upon lysis of the producing cell[2]. T6SSs deliver effectors to target cells while still bound to a membrane[17,19–21].

The genome-wide prediction of 631 eCIS-like co-translational assemblies by Chen et al. revealed a complex genetic landscape of eCISs[1], identifying an eCIS-like operon in the genus *Salmonella*[1]. *Salmonella enterica*, a Gram-negative, flagellated, rod-shaped enterobacterium[22], includes subspecies *salamae* and *diarizonae*, both of which encode eCIS-like operons, identified in 143 *salamae* strains[1]. These two subspecies are typically isolated from environmental sources, such as soil samples, and occasionally reptilian guts[23,24]. *S. salamae* has been known to cause opportunistic infections in immunocompromised patients[25]. Notably, *salamae* subspecies have evolved to survive outside of their host, compared to pathogenic serovars[24].

Here, we report the atomic structure of an eCIS-like CIS in *Salmonella*, including its membrane-associated component. We then apply structural analysis to demonstrate how the *Salmonella* CISs (SalCIS) may deviate from canonical eCISs by anchoring to the inner membrane. We leverage structural insights to identify, to the best of our knowledge, previously unannotated and uncharacterised operons of bacterial CISs. Finally, we characterise putative effectors present in the operon. Understanding these mechanisms may provide deeper insights into the evolutionary and functional diversity of CISs in pathogenic bacteria.

Results and discussion

SalCIS is a contractile injection system with conserved CIS architecture

We confirmed the presence of an eCIS-like operon in *Salmonella enterica* subspecies *salamae*. The operon present in *Salmonella* species is a co-translated bidirectional operon, comprising eighteen open reading frames (Fig. 1a)[1]. Bioinformatic analysis identified four strains of *Salmonella enterica* subsp. *salamae* encoding a CIS cassette[1] (SalCIS). Out of these operons, the operon from strain NCTC9936 was selected for further study due to continuous translation sequences. The Afp nomenclature (Afp1 to Afp16) was used to assign a putative function to all hypothetical proteins (SalCis1-15). The putative packing AAA ATPase SalCis15 is encoded upstream of the putative effector proteins SalCgo1 and SalCgo2 (Fig. 1a). According to previous eCIS classification[1], SalCIS falls into clade Ib, which includes AlgoCIS from the marine bacterium *Algoriphagus machipongonensis* and the T6SS subtype IV (T6SS^{iv}) from *Amoebophilus asiaticus* (Fig. 1a). Notably, a putative protein, SalCis20, was predicted to have transmembrane helices, and a domain, with conserved homology to peptidoglycan hydrolases (Supplementary Fig. 1a–c). The SalCIS operon codes for a putative tail fibre-like protein, SalCis13, with conserved protein sequence homology to proteins in the operons of *Amoebophilus asiaticus* and other CISs[17,26]. To understand the SalCIS system via structural analysis, we constructed a deletion mutant of the SalCIS operon (ΔSalCis13-ΔSalCis20). The mutant was cloned, heterologously expressed in *E. coli* and purified for cryo-electron microscopy (cryo-EM). We obtained maps at global resolutions of 2.86 Å (baseplate), 2.3 Å (extended sheath) and 2.97 Å (cap) (Fig. 1c–f). The density was excellent throughout, apart from a tapering off in resolution towards the edges of the baseplate maps, and allowed model building (Supplementary Table 1). Though detected in LC-MS/MS data of the entire operon (Fig. 1g, Supplementary Table 2), SalCis15 was absent from all maps, in line with a transient association with SalCIS, as noted in other CIS[10,15].

SalCIS is composed of a baseplate, a helical outer sheath, an inner tube complex, and a terminal cap, typically 600 nm in length and 18 nm in diameter (Fig. 1a). The baseplate surrounds the central spike through a cage and compact wedge complexes that transition into the sheath and tube (Fig. 1e insets). The extended sheath and tube complex assembly interacts with the cap (Fig. 1f). The structure of this CIS preserves key features noted in other CISs, such as bacteriophages, T6SSs, and previously described eCISs (Supplementary Table 3).

The SalCIS inner spike retains the structure of eCISs such as AlgoCIS and tCIS, with a SalCis8 trimer, and capped by a single PAAR-like SalCis10 at its C-terminus (Fig. 2a)[27]. The T4 bacteriophage gp27- and gp5-like domains of SalCis8 are also retained (Supplementary Fig. 2a, b). The gp5-like helix of SalCis8 is about 27 Å longer than eCISs like PVC and Afp and instead resembles the spike arrangement of clade Ib eCISs (Fig. 2b). The gp27-like domain of one SalCis8 monomer interacts with the proximal end of two copies of SalCis7 primarily through electrostatic interactions, via defined residues. The LysM domains of SalCis7 stabilise the spike through contacts with SalCis8 (Supplementary Fig. 2c). The putative plug protein, SalCis6, encoded with an alternative start codon (Val), is inferred by LC-MS/MS data, when the entire operon is expressed (Supplementary Table 2). Its complete density could not be resolved, due to particle scarcity, only α-carbon chain loops that correspond to the residues 49–56 of the AlphaFold3 model were traced within the lumen (Fig. 2c), indicative of a conserved spike plugging mechanism in SalCIS[4].

The spike assembly is surrounded by a cage, including hexameric assemblies of both SalCis11 and SalCis12, forming a conserved trifurcation unit akin to that of the baseplate of the bacteriophage T4 and other eCISs (Supplementary Fig. 3a)[6,8]. SalCis11 and SalCis12 display gp6 and gp6/7-like folds, respectively[6,8] (Supplementary Fig. 3b–d). SalCis11's domain I extensively interfaces with SalCis12's domains I and IV via α-helical contacts (Fig. 2d). Notably, SalCis11 harbours an extension of domain IV that was not identified in other CISs (Fig. 2e). Surface analysis of the seven α-helices (residues 419–549) comprising this domain revealed a distinct charge distribution, coupled with a hydrophilic character (Supplementary Fig. 3e).

SalCis12 is deficient in a large extension of domain V, as is present in Cis12 from tCIS, and extended in comparison to its homologue Alg12 from AlgoCIS (Fig. 2f), resulting in a compact baseplate wedge, nearly hexagonal in shape in SalCIS (Supplementary Fig. 3a). SalCis12 is instead homologous to the predicted structure of the putative cage proteins of *A. asiaticus* (Fig. 2f). In *A. asiaticus* T6SS^{iv}, injection systems form bundles[17]. We noted the presence of CIS aggregates in our TEM analysis (Supplementary Fig. 4a). It is plausible that the compact nature of the *Salmonella* CIS baseplate facilitates the occurrence of these injection systems in bundles wherein the baseplate may interact with the inner membrane. The outer surface of the baseplate is dominated by positive charges and hydrophilic character, around the circular tip formed by the extended domain IV (Supplementary Fig. 3e). The distal tip is also positively charged. The combination of positive charge with hydrophilic character likely facilitates membrane interaction[3,16,28]. Taken together, our analysis indicates that the SalCIS baseplate may be a membrane-interacting variant. It combines conserved eCIS architecture with a more compact geometry, forming bundles. Electrostatic charges around the baseplate are favourable for interacting with a membrane, with conserved homology closer to clade Ib eCISs.

SalCis2 constitutes the outer sheath vertex of SalCIS

SalCis2, the sole sheath component of SalCIS, is divided into four domains (Fig. 3a). An X-loop domain was resolved, to the best of our

https://doi.org/10.1038/s41467-026-71989-6

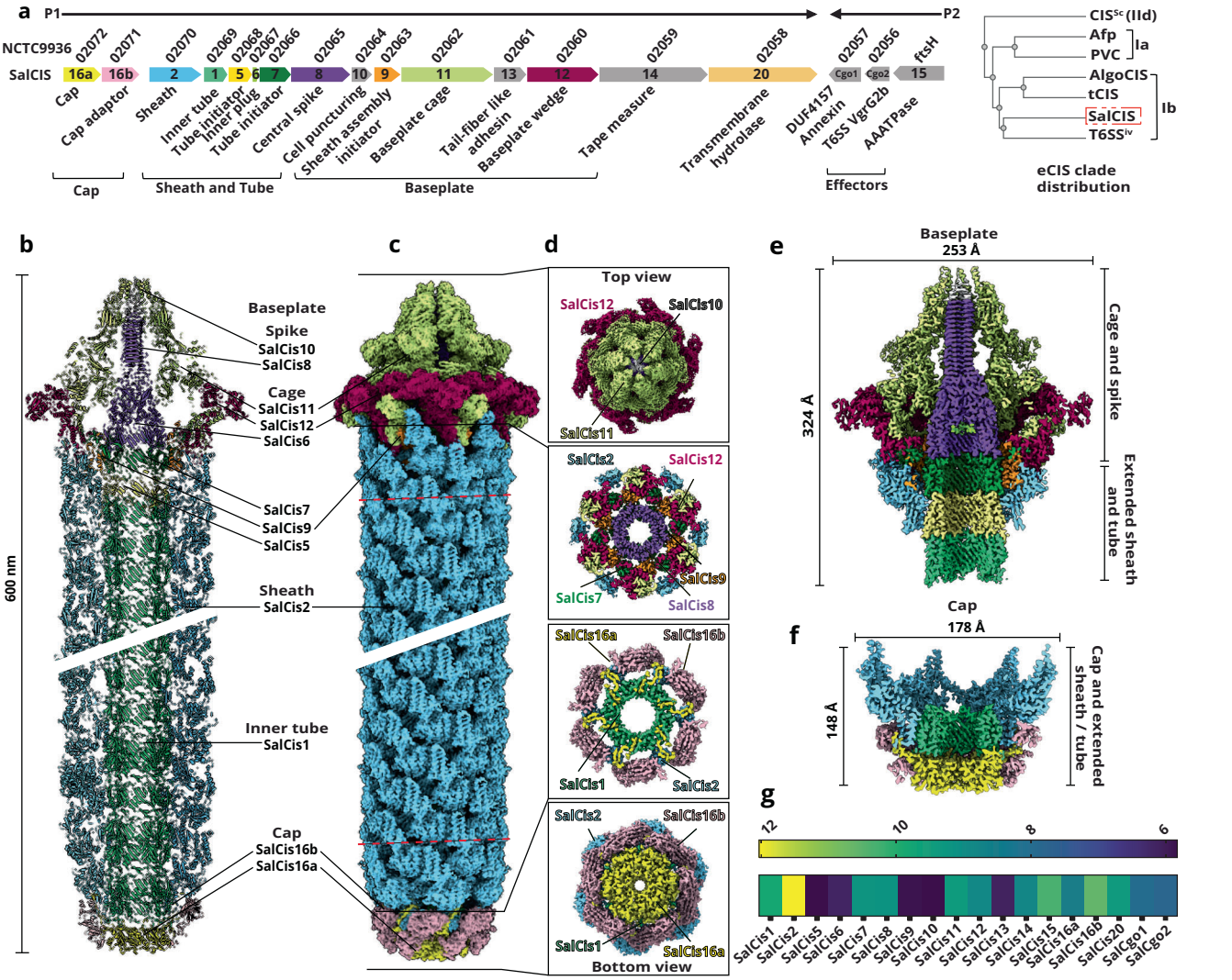

Fig. 1 | Atomic structure of the *Salmonella* CIS. a *Salmonella* CIS (SalCIS) cassette, with genes annotated according to the NCBI genomic database identifiers, and numbered according to the antifeeding prophage nomenclature. Descriptors of genetic components are presented according to resolved densities; all coloured components were fully or partially resolved in cryo-EM maps, and grey components were not. The text under the brackets indicates assemblies and/or functions confirmed in this study. P1 refers to the first natural promoter identified, and P2 refers to the second one. Right panel shows the placement of SalCIS (red rectangle) within the eCIS clade organisation. **b** Atomic structure of SalCIS as cartoon representation, clipped at the centre vertically to reveal tube and central spike features. Model depiction is a stitched representation of symmetry copies of constructed atomic models expanded onto the cryo-EM structure. **c** SalCIS cryo-EM density. The map shown is a composite map constructed by merging three separate maps, dashed red lines indicate borders where maps were stitched, σ (map contour level) for each map is reported in Supplementary Figs. 17, 18. **d** Boxed lateral insets show cross-sectional slice views illustrating the arrangement and interactions of various SalCIS proteins within the baseplate and cap complexes. **e** Clipped view of the SalCIS baseplate complex cryo-EM map, highlighting individual units and interactions between the baseplate components, comprising the outer cage (SalCis11 and SalCis12) and the inner spike and puncture complex with the tube and sheath vertex (SalCis10, SalCis8, SalCis6, SalCis7, SalCis5, SalCis2 and SalCis1). **f** Clipped view of the SalCIS cap complex cryo-EM map highlighting individual units and interactions of the terminal cap complex with the inner tube (SalCis16a, SalCis16b, SalCis2 and SalCis1). **g** LC-MS/MS coverage when all SalCIS proteins are expressed and purified, heat map shows $\log_2$ of unique spectral counts of all proteins present, reported in Supplementary Table 2, coloured according to key.

knowledge, not previously noted in eCISs. The X-loop forms salt bridges between Asp322–Arg84 (P3) and Lys43 (P4), of two sheath protomers (Fig. 3bi), stabilising the extended conformation. Domain III includes two α-helices and a disordered loop, distinctly oriented flush parallel with the sheath wall (Supplementary Fig. 5ai). The sheath adopts a helical symmetry, with a rise of 39.2 Å and a twist of 21.6 °. Sheath assembly is stabilised by a conserved C-terminal donor strand exchange (DSE) motif. The N-terminus of each SalCis2 monomer (P3) engages in a tripartite DSE motif, forming between protomers 1 and 2, previously noted in tCIS (Supplementary Fig. 5aii, iii). Three distinct conformational states of SalCis2 are observed, which we label R1-3 (Supplementary Fig. 5b). The C-terminus of R1 shifts (residues 507–516) to accommodate DSE with SalCis9, distinct from R2/R3. The R1 N-terminus also shifts to connect with the helical SalCis2-R2 (Supplementary Fig. 5b). Comparative analysis revealed SalCIS shares distant homology with Alg2, Cis2 (tCIS), and *Streptomyces* Cis2 (Supplementary Fig. 5c). The AlphaFold3 structural prediction of the *A. asiaticus* sheath protein (ACE06419.1) is predicted to harbour the X-loop, but it does not retain the vertical helix-loop-helix motif orientation (Supplementary Fig. 5d). We postulate that the X-loop feature assists in stabilising the entire helical outer sheath complex, in an extended state. Structural homology searches revealed a cluster of hits, with single sheath protein CISs, structurally identical to SalCis2 (Supplementary Fig. 6a, b).

https://doi.org/10.1038/s41467-026-71989-6

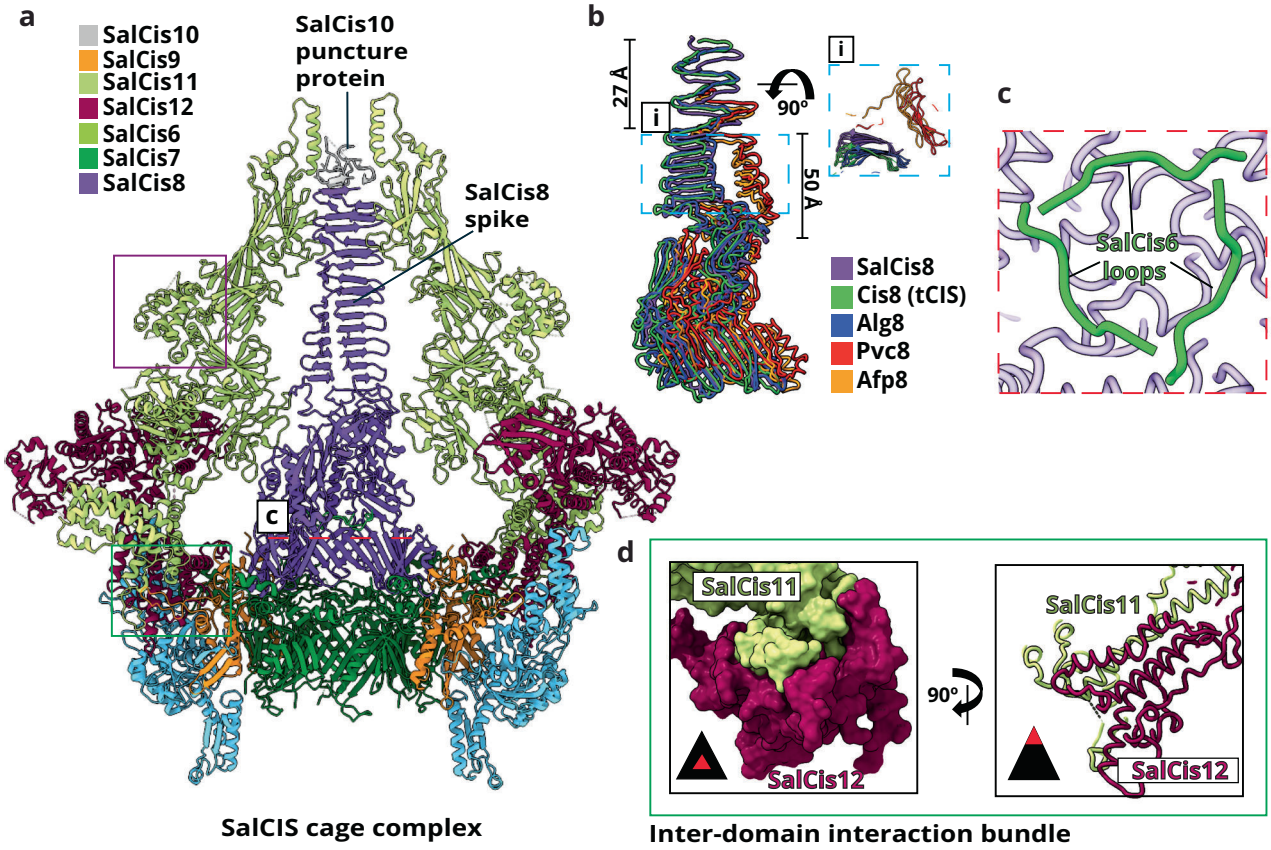

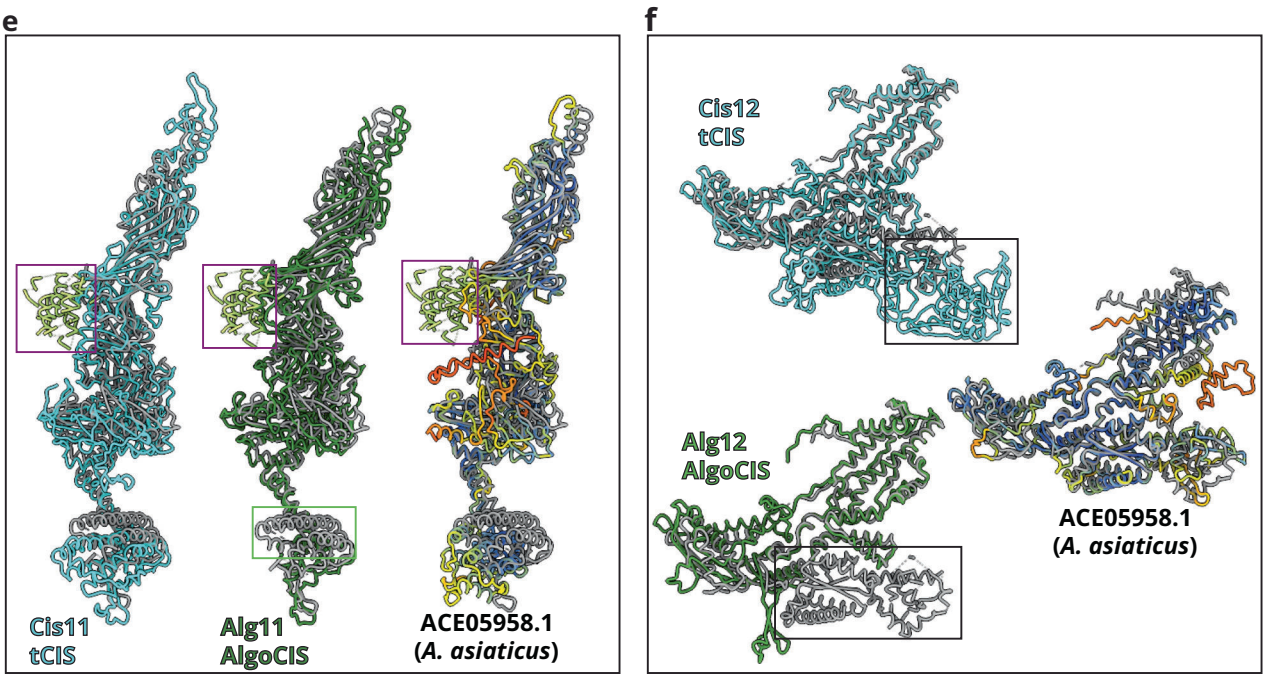

Cryo-EM reconstruction of the contracted sheath informed an estimate of 272 nm length (Supplementary Fig. 7a, b). This estimate would result in moving the inner tube forward by a distance of ~328 nm. Sufficient for piercing *S. enterica salamae's* own double membranes[29] (Supplementary Note 1).

SalCis1 is highly conserved; superimposition of SalCis1 with Alg1, Afp1, Cis1 from *Streptomyces*, Pvc1, and Cis1 reveals strong structural similarity. So does the comparison of SalCis1 with the structure prediction of the *A. asiaticus* Hcp component (Supplementary Fig. 8a–d).

Taken together, our analysis of the tube and sheath complex shows that the inner tube of CIS's, including SalCIS, seems to be highly conserved, but the tail sheath of SalCIS appears to have acquired some adaptations that might have important functional roles.

Fig. 2 | Details of the spike-puncture complex. a Cartoon depiction of SalCIS inner spike and cage complex, chains are coloured according to key. Surrounding chains are hidden to reveal interaction details. Red dashed line highlights features detailed in inset c. Green box highlights features detailed in inset d. Purple box highlights feature compared in inset e. **b** Cartoon depiction of the SalCis8 spike structure, highlighting conserved domains. Blue dashed box shows a top-down view of the spike (i). Various spike proteins are coloured by key. **c** SalCis6 viewed within the inner lumen of SalCis8, from the perspective of the red dashed line in (**a**). Depicting three loops traced within the spike density, corresponding to the AlphaFold3 model of SalCis6. **d** Shows domains I and IV from SalCis12 interacting with SalCis11's domain I via α-helices. Left panel depicts electrostatic surface depiction of the solved structure, right panel depicts side view of the same in chain format. **e** SalCis11 has an extension, as shown by superimposition of the solved structure of SalCis11(in grey) onto homologues, purple boxes indicate an extension of the cage (coloured green), only present in SalCis11. Green box indicates the helical extension of SalCis11's domain missing in AlgoCIS. **f** SalCis12 is related to other CISs as illustrated by the superimposition of the solved structure of SalCis12 (in grey) onto homologues. Black box around Cis12 from tCIS indicates a large domain extension not present in SalCis12, black box around SalCis12 extended domain indicates extension of domain in SalCis12, not present in AlgoCis12. The predicted structure of the SalCis12 homologue in *A. asiaticus* highlights high structural similarity. The *A. asiaticus* cage protein homologues are AlphaFold-predicted structures coloured by pLDDT confidence scores, where blue indicates high confidence and orange/red indicates low confidence.

SalCis16b is the cap adaptor of SalCIS sheath vertex

The first gene in the *S. enterica* SalCIS operon, SalCis16a, forms a hexameric cap structure with an opening of 15 Å between the distal-most helical loops (residues 143–155). This is wider than the opening reported in the distal loops of the single cap-protein assembly of the Afp cap, belonging to clade Ia eCIS[16]. In contrast to clade Ia eCIS, a second hexamer forms the complete cap in SalCIS, via the terminal cap adaptor, SalCis16b (Fig. 3c). Previously, a double cap assembly was reported in the AlgoCIS and tCIS (both clade Ib), with similar dimensions[3,4]. Deletion of SalCis16b resulted in disrupted particle assembly, and the formation of tube–baseplate complexes (Fig. 3d). Negative-stain TEM revealed low-energy assemblies of the sheath protein SalCis2, with no extended or contracted sheath conformations assembled on the baseplate (Fig. 3d). The final DSE interaction, between SalCis2 and the cap, is stabilised by the N-terminus of SalCis16b, the cap adaptor. Here, the SalCis2-R3 conformation engages in a terminal DSE motif with SalCis16a (Fig. 3e). The N-terminus of SalCis1's final six protomers shows a distinct change in conformation upon binding SalCis16a (protomer 2, Supplementary Fig. 8e). Similar differences in conformation of SalCis1 homologues have been reported in eCISs such as the Afp[16].

Together, these interactions define an ordered cap assembly, where SalCis16b anchors SalCis2 via the terminal DSE, closing the sheath-tube complex.

SalCis20 is an integral membrane protein containing a putative hydrolase domain

SalCis20 was predicted to have three transmembrane α-helices and a Sec-type signal sequence with a cleavage site predicted at residue 42 (Fig. 4a)[30]. Cryo-EM analysis of LMNG-solubilized SalCis20, expressed and purified recombinantly as a membrane protein in *E. coli*, resulted in a 2.73 Å resolution map of the homodimer. Each monomer contains three transmembrane α-helices, embedded in the detergent micelle, and a large periplasmic domain (Fig. 4b, Supplementary Table 1, and Supplementary Fig. 9). Residues 1–42 were absent in the in-gel mass spectrometry analysis of the purified protein, which may indicate post Sec-mediated export cleavage[31] (Fig. 4a, Supplementary Fig. 9). The postulated periplasmic domain adopts a conserved hydrolase fold, homologous to SleL (PDB: 4s3j), a cortical spore lytic enzyme from *Bacillus cereus*[32] (Fig. 4c), with conservation of several residues in the catalytic core (Fig. 4d, RMSD 0.976 Å). SleL is an N-acetylmuramoyl-L-alanine amidase, which cleaves peptidoglycan[32]. Given the similarity of *Salmonella* and *Bacillus* peptidoglycan composition[33], we propose that SalCis20 may have a role in remodelling the cell wall, to assist SalCIS insertion, analogous to MltE insertion by *E. coli* T6SS[34]. Inspected genomes of CIS clade Ib and structure-based searches[35] revealed putative homologues of SalCis20, with similar signal sequences, topologies and domains (Supplementary Fig. 1a–c)[36–38].

SalCIS localises in proximity to the inner bacterial membrane

To examine SalCis20 localisation, we imaged live *Salmonella* cells expressing SalCis20 fused at the C terminus to the fluorescent reporter, mKate2. Fluorescence microscopy revealed a peripheral signal of the SalCis20-mKate2 fusion, consistent with membrane association (Fig. 5a). Removal of the N-terminal Sec-type signal sequence (Δ-Nterminal-aa1–42-SalCis20-mKate2) resulted in a diffuse cytoplasmic fluorescence (Fig. 5b). Consistent with the predicted membrane topology, this indicates that SalCis20 associates with the cell envelope in a signal-sequence-dependent manner.

To investigate in situ localisation, the operon was heterologously expressed in a minicell-producing strain of *S.* Typhimurium. Here, the entire SalCIS operon was expressed. The reconstructed tomograms revealed CIS localising close to the inner membrane of minicells (Fig. 5c). The number of CIS observed per bundle varied between 1–10, measuring between 600–700 nm in length, and a uniform width of 18 nm per CIS, congruent with the extended SalCIS diameter from SPA analysis. Notably, SalCIS expression in minicells led to arrested cell division. The inner membrane appeared pinched when in proximity of SalCIS (Fig. 5c). This localisation is reminiscent of what has previously been described for the cryo-ET analysis of the *Amoebophilus asiaticus* T6SS^{iv}.

Structural modelling suggests SalCis13 may act as a membrane-associated anchor

SalCis13 is the putative tail fibre of SalCIS. Structure-based searches revealed highly conserved homologues (Supplementary Fig. 10a). AlphaFold3 modelling of SalCis13 as a trimer was more favourable than other oligomeric states tested, predicting a distinct trimer, compared to canonical eCIS tail fibres (Supplementary Fig. 10b). Structural similarity was noted when compared to the AlphaFold3 predicted structures of homologues to SalCis13 in *A. asiaticus* T6SS^{iv}[17] and *Aureispira* CCB-QB1 CIS operons (Supplementary Fig. 10b). The baseplate of SalCIS was docked into the sub-tomogram averaged structure of the *A. asiaticus* and *Aureispira* CCB-QB1 CISs' sub-tomogram averages, revealing similar geometry (Supplementary Fig. 10c). AlphaFold2 Multimer predicted modelling of SalCis13, SalCis20, and SalCis11 as a complex suggests a transient interaction. We postulate that the C-terminal TMDs of SalCis20 could engage six trimers of SalCis13, which in turn may associate with SalCis11 via the N-terminus of SalCis13 (Supplementary Fig. 10d).

Expression of the full SalCIS operon in *E. coli* and *S. enterica* yielded mostly aggregated or disassembled particles, unsuitable for structural analysis (Fig. 4e, Supplementary Figs. 4, 11). LC-MS/MS analysis of the entire operon expressed, detected SalCis20 post purification at a relative abundance of 0.004, normalised to the cap protein SalCis16b at 1.0 (Supplementary Table 2). The low abundance may indicate dissociation during lysis, reminiscent of the membrane-associated complex in T6SSs[39]. Deletion of SalCis13 and SalCis20 individually did not improve particle yield or quality (Supplementary Fig. 11b). The double deletion mutant (ΔSalCis13-ΔSalCis20) yielded the highest proportion of intact particles and enabled high-resolution single particle reconstruction (Fig. 4f).

Our predicted structure analysis of SalCis13 and experimental structure of SalCis20 was used to guide the hypothesis of how

https://doi.org/10.1038/s41467-026-71989-6

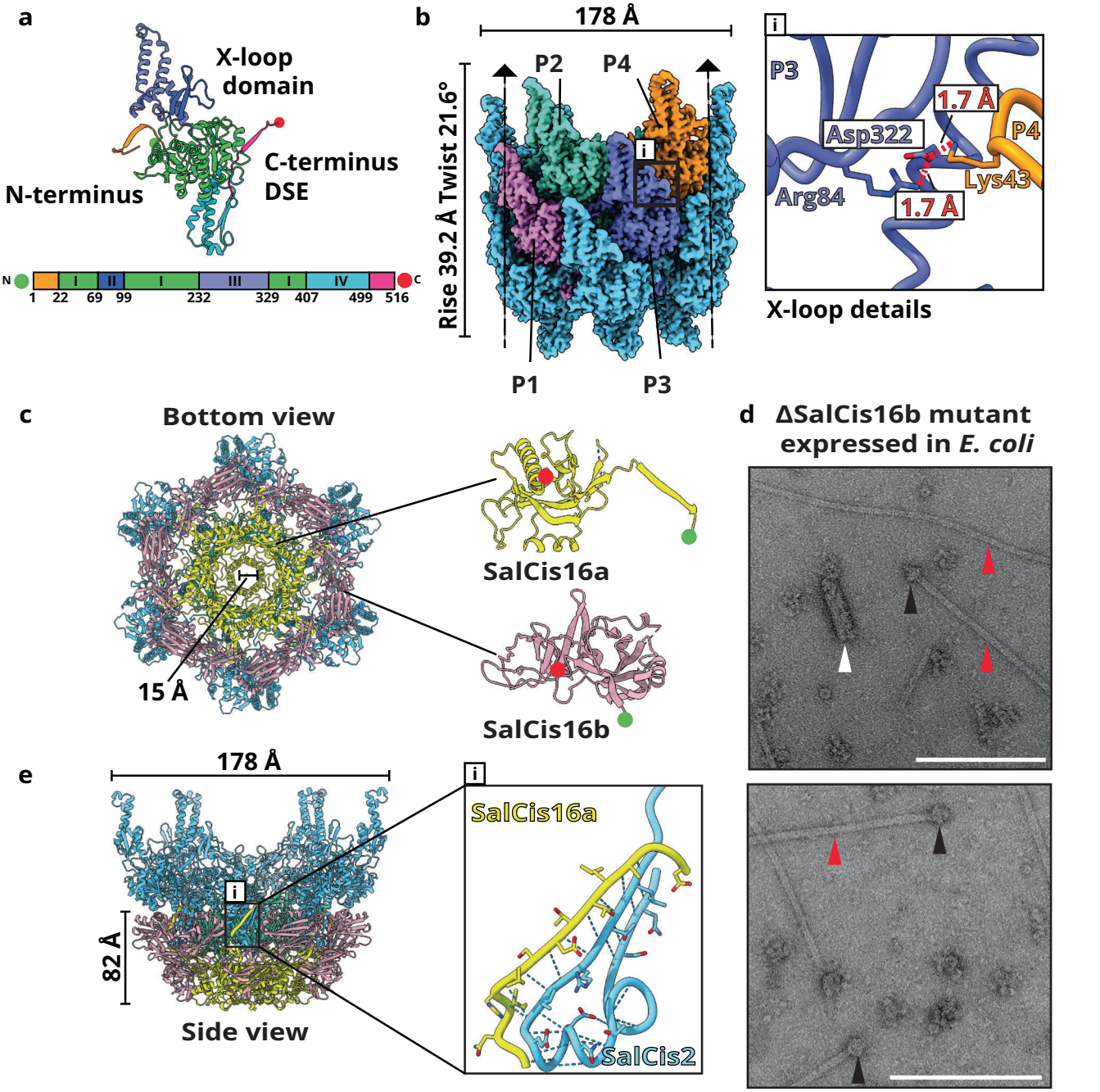

Fig. 3 | Outer sheath and tube terminate at the cap. a Domain organisation of SalCis2. The N-terminus donor strand exchange (DSE) domain is coloured orange, the C-terminus DSE is coloured pink. **b** Details of outer sheath assembly. Four protomers (P1-P4) are highlighted and colour-coded. Vertical dashed lines indicate the vertex wall, and arrowheads point towards the baseplate. (i) Shows details of the X-loop motif, key residues are highlighted, and atomic distances are marked. **c** Hexameric structure of the SalCIS cap shown in cartoon format, viewed from the bottom. N- and C-termini (red and green, respectively) of SalCis16a and SalCis16b monomers are indicated, the structures are shown in cartoon format. **d** Negative-stain TEM images of a ΔSalCis16b mutant expressed in *E. coli*, purified by gradient fractionation. Black triangles indicate baseplate regions of tube–baseplate complexes; red arrows mark polymerised inner tube complexes; white arrow shows low-energy sheath assemblies. The experiment was repeated twice with similar results. Scale bar, 200 nm. **e** Cartoon depiction of the SalCIS cap structure. Coloured box indicates zoomed-in views of key contact sites. (i) Top box shows a model of structural interactions between the final DSE motif between the SalCis2 tube and SalCis16a, polar residues and hydrogen bonds are highlighted.

SalCIS may interact with the inner membrane (Supplementary Fig. 10d)[40].

Canonical secretion or particle release was not detected in SalCIS

We engineered a deletion strain of *S. enterica* subsp. *salamae*, ΔSalCIS, and reintroduced the full operon on inducible plasmids, to characterise SalCIS-mediated secretion or particle release. Here, the SalCIS operon was co-expressed. Upon induction, neither the sheath protein SalCis2 nor the Hcp homologue SalCis1 could be detected in the extracellular fraction. Furthermore, the two putative effectors were not detected in the extracellular fraction under the tested conditions. Proteins were only detected in the cellular fraction, probed via specific polyclonal antibodies (obtained through GenScript) using

https://doi.org/10.1038/s41467-026-71989-6

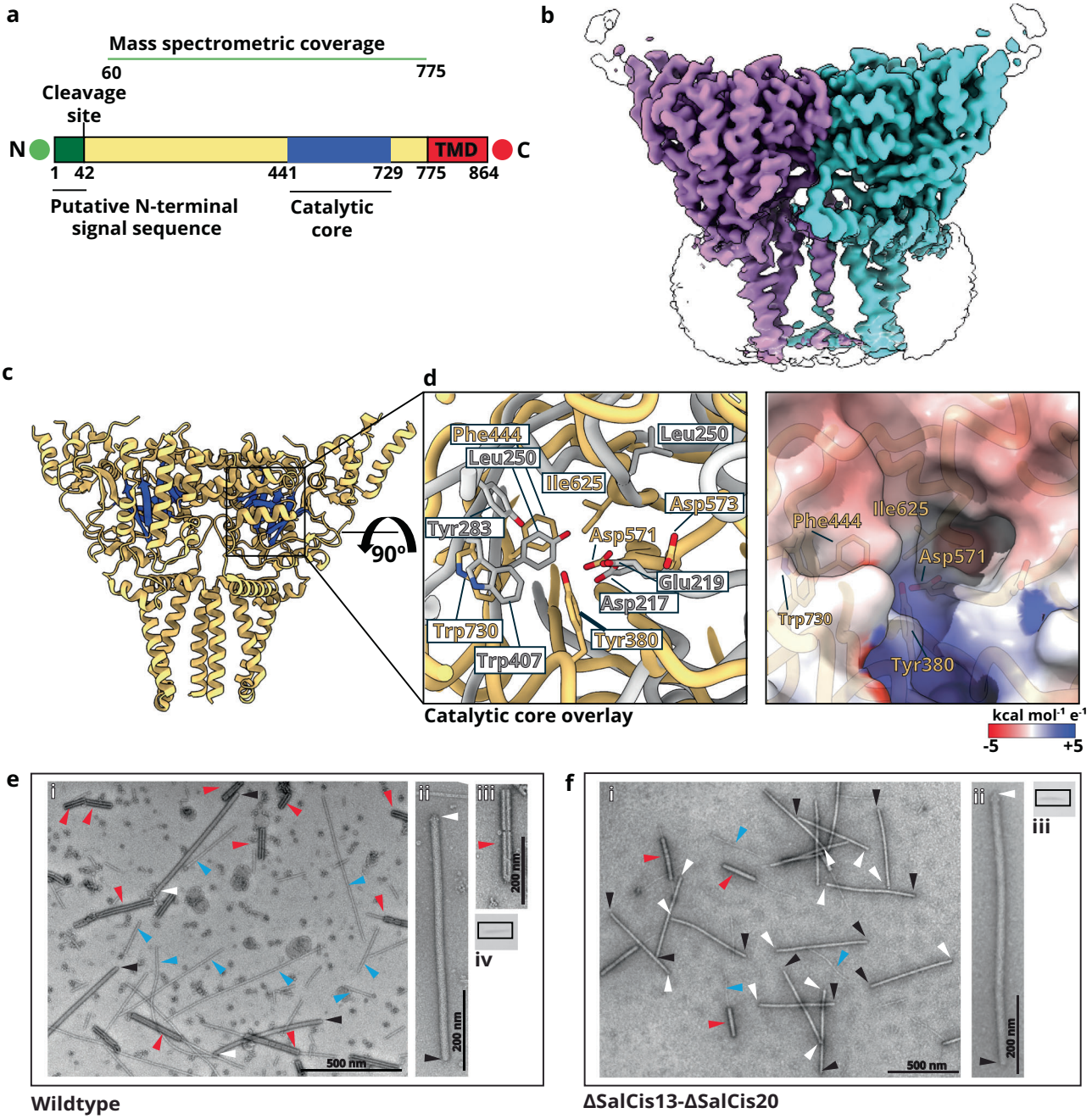

Fig. 4 | Cryo-EM reveals the structure of an integral membrane protein in SalCIS. a Predicted domain organisation of SalCis20. Bioinformatic analysis shows an N-terminal Sec-type signal sequence (cleavage after residue 42), three TM α-helices per monomer, and a large periplasmic domain (residues 44–775) green bar indicates mass spectrometric coverage (60–775), transmembrane domain is indicated (TMD). **b** Cryo-EM structure of LMNG-solubilized SalCis20, expressed and purified recombinantly in *E.coli*, σ (map contour level) 3.61. Reconstruction reveals a homodimer, with transmembrane helices embedded in a detergent micelle and a large periplasmic domain extending into the solvent, each monomer coloured. **c** Solved structure of SalCis20 homodimer, highlighting the two catalytic cores in blue. **d** Left panel shows structural alignment of the catalytic cores from *B. cereus* SleL (grey) and *S. enterica* SalCis20 (yellow), highlighting conservation within the catalytic domain. Right panel shows a negative electrostatic surface charge localised in the putative substrate binding core. **e** Negative stain images of the wildtype SalCIS operon expressed and purified in *E. coli*. Black arrowheads point at caps, white arrows point at baseplates, red arrows denote contracted sheath assemblies, and blue arrows denote expelled inner tubes. (i) Low magnification image of diluted final preparation of heterologously expressed wild-type SalCIS in *E. coli*. (ii) Magnified view of one extended SalCIS particle. (iii) Magnified view of contracted sheath assembly. The experiment was repeated thrice with similar results. **f** Negative stain images of the ΔSalCis13-ΔSalCis20 mutant of SalCIS expressed and purified in *E. coli*. Labelled the same as e. (i) Low magnification image of diluted final preparation. (ii) Magnified view of one extended SalCIS particle. Western blot band indicates presence of SalCis2 at 57 kDa in e (iv) and f (iii), probed with an anti-SalCis2 specific antibody, cropped for clarity (Source Data Fig. 4e, f). The experiment was repeated twice with similar results.

Western blot (Supplementary Fig. 12a–c). While regulated secretion (similar to T6SSs) or particle release (as for eCIS) cannot be excluded, the absence of detectable proteins supports a non-canonical or potentially domesticated/defensive role, involving an alternative activation pathway.

SalCIS expresses effectors toxic to bacteria

Within the SalCIS operon, we identified two putative effectors, SalCgo1 and SalCgo2, positioned near the AAA ATPase, SalCis15. For LC-MS/MS analysis, the SalCIS operon was co-expressed in *E. coli*. SalCis1–20 were expressed on a pBAD33 plasmid, whereas SalCis15, SalCgo1 and

https://doi.org/10.1038/s41467-026-71989-6

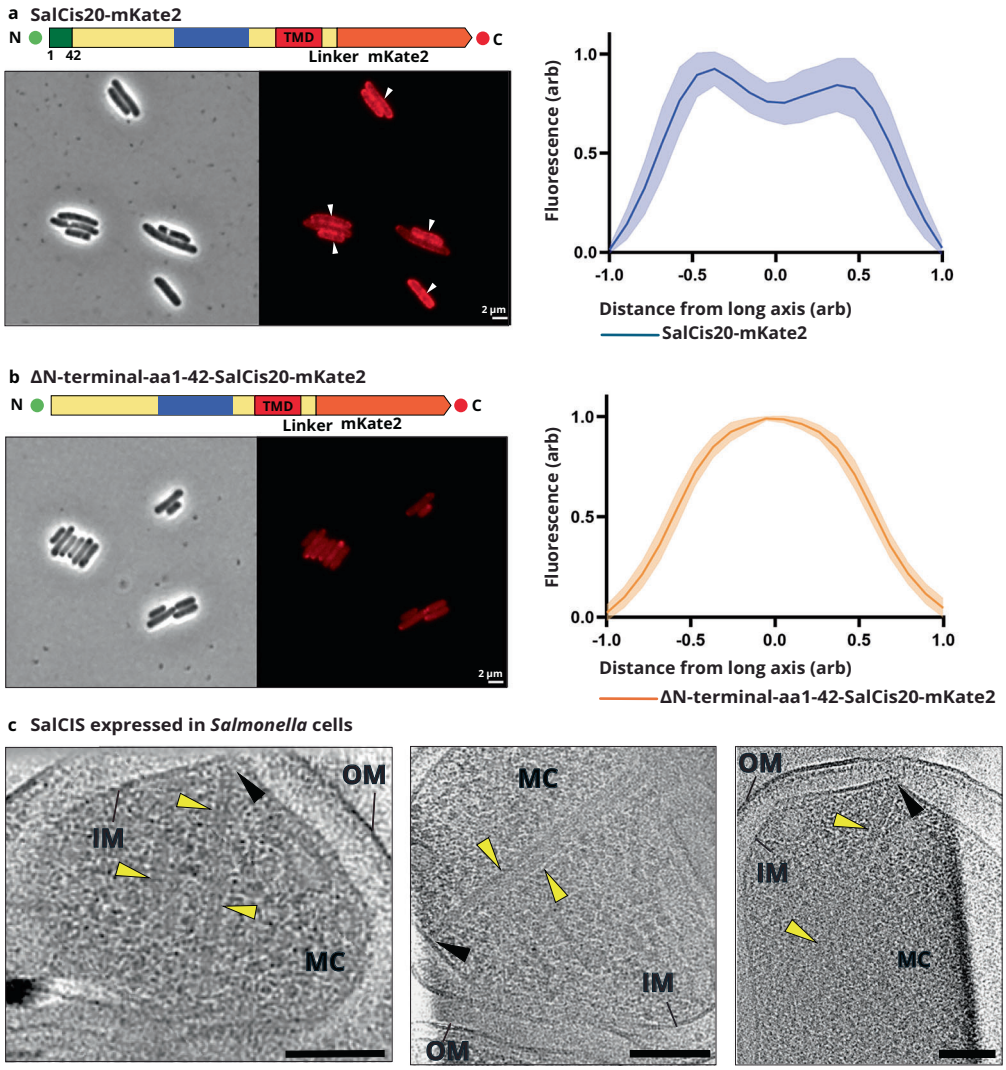

Fig. 5 | Localisation of SalCIS in-situ. a Left panel shows epifluorescence microscopy of *S.* Typhimurium cells heterologously expressing SalCis20 C-terminally tagged with mKate2, green bar indicates signal sequence, blue bar indicates the putative catalytic core, red bar indicates the transmembrane domains (TMD), and the orange bar indicates an mKate2 tag. White arrows point to peripheral fluorescence, showing that the protein associates with the membrane. The right panel shows the intensity profile; both axes are in arbitrary units (arb), reflecting raw pixel distance and detector counts, respectively. Data are presented as mean values ± SD, $n = 21$ cells. **b** Left panel epifluorescence microscopy of *S.* Typhimurium cells heterologously expressing a mutant of SalCis20 C-terminally tagged with mKate2, and a deletion of the N-terminus SEC type secretion signal, blue bar indicates the putative catalytic core, red bar indicates the transmembrane domains (TMD), and the orange bar indicates an mKate2 tag. Fluorescence is diffusely distributed across the cytoplasm, indicating loss of membrane localisation. Right panel shows the intensity profile. Data are presented as mean values ± SD, $n = 20$ cells. Epifluorescence microscopy data is presented in the Source Data file, the experiment was performed once. **c** Three individual, reconstructed cryo-electron tomogram slices, from three separate cells, illustrating key features. Minicells (MC) are imaged, and yellow arrows highlight SalCIS bundles positioned within the cytoplasm. The inner (IM) and outer (OM) membranes of the Gram-negative *S.* Typhimurium cell are labelled. The black arrow denotes potential interaction between SalCIS structures and the inner membrane. Black scale bar, 100 nm.

SalCgo2 were expressed on a pET-11a plasmid. After purification, both putative effectors were detected by LC-MS/MS in a gradient-separated preparation, together with the core components of SalCIS, consistent with their retention, at least in some of the particles, during complex isolation (Supplementary Table 2).

Structure prediction of SalCgo1 and SalCgo2 identified a conserved HEXXH motif, demonstrating similarity to the C-terminal metalloprotease domain of the T6SS effector of *Pseudomonas aeruginosa* (PDB: 6H56) VgrG2b[41], previously implicated in periplasmic toxicity in *E. coli*[41]. A conserved DUF4157 domain was also identified in SalCgo1, previously found adjacent to eCIS-associated toxins (EATS) targeting bacterial or fungal non-kin microbes[42,43] (Supplementary Data 1).

To test for toxicity, the putative effectors were cloned separately into a pET-11a vector and expressed in a pLysS plasmid-harbouring strain of *E. coli*. Mild periplasmic toxicity of SalCgo2 in *E. coli* was noted when expressed with an N-terminal *OmpA* gene fusion to direct SalCgo2 to the periplasm[44] (Supplementary Fig. 13a). SalCgo2 was not toxic when expressed in the cytosol (Supplementary Fig. 13a, Wt-OmpA-SalCgo2). Periplasmic toxicity was abolished by a triple point mutation in the HEXXH motif (H99A, E100A, H103A), as well as by the E100A single substitution.

In contrast, SalCgo1 was toxic upon periplasmic and cytosolic expression. HEXXH motif mutations (H150A, E151A, H154A), N- or C-terminal truncations, and a single E151A mutation failed to abolish toxicity (Supplementary Fig. 13b).

Co-expression of both effectors, expressed in tandem with and without the *OmpA* gene fusion, did not abolish toxicity (Supplementary Fig. 13c), and no cognate immunity protein was identified. SalCgo2 was less toxic compared to an established periplasmic toxin, Tse1

https://doi.org/10.1038/s41467-026-71989-6

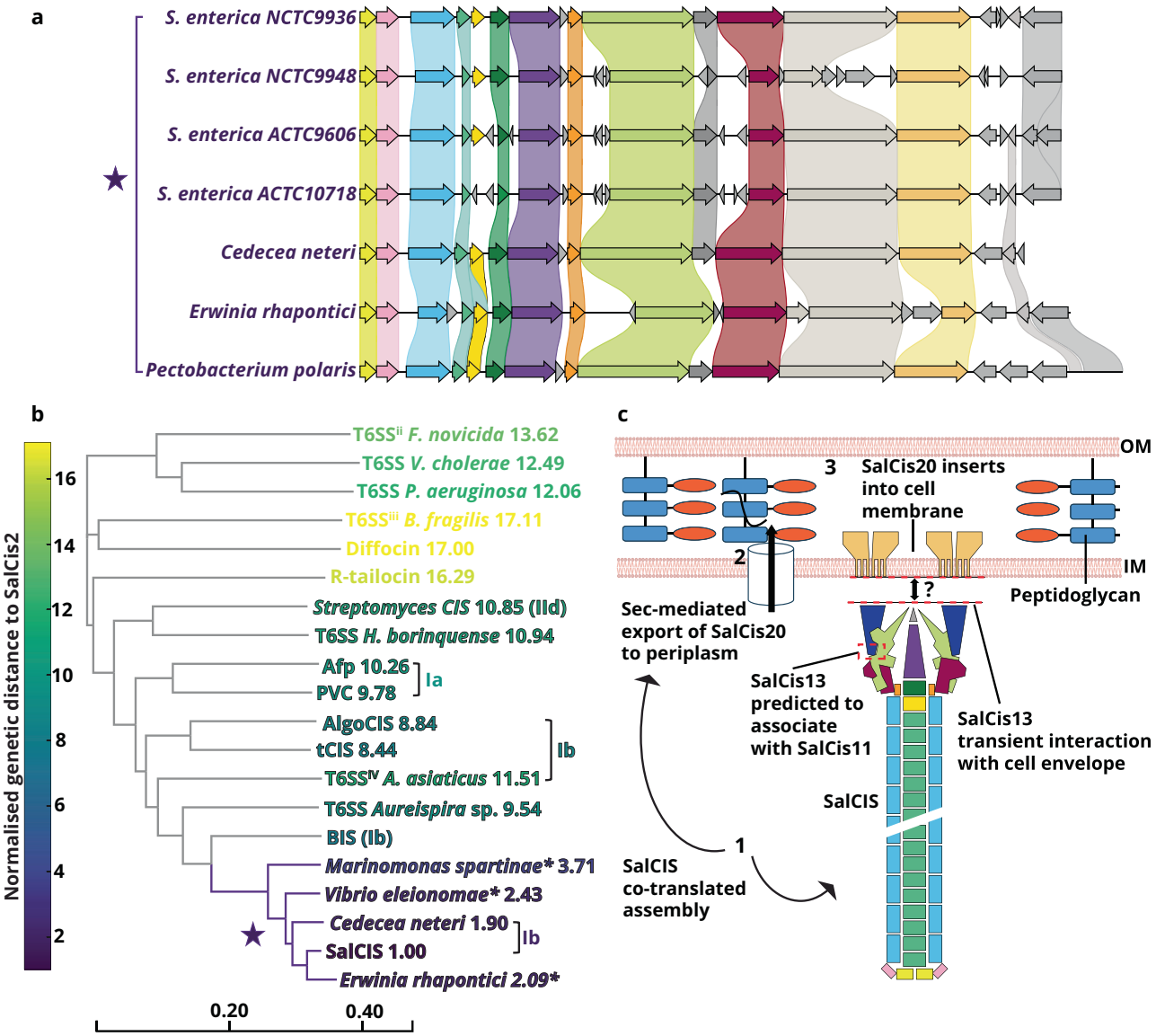

Fig. 6 | Evolutionary context of SalCIS. a Gene cluster alignment of four SalCIS operons and related clusters in other bacteria employing Clinker. Genes are coloured according to SalCIS homology. Asterisk indicates similar CIS operons **b** Phylogenetic tree of CIS sheath proteins based on multiple sequence alignment (MSA) performed using Clustal Omega[65]. Branch lengths were normalised to the SalCis2 (set as 1.0) to enable relative comparison of divergence. eCIS clade lineages are mentioned in brackets or grouped. An asterisk indicates sheath proteins from unannotated eCIS operons identified in this study. **c** Cartoon depiction of the postulated mode of inner membrane (IM) anchoring in SalCIS; OM, outer membrane. Once all components of the operon are expressed, SalCis20 is exported to the periplasm via a Sec-mediated translocation pathway (1). The signal sequence cleaves as Sec-translocon recognition results in membrane-embedded TMDs (2). SalCis20 may form a transient interaction with SalCis13 and the SalCIS baseplate, transiently contacting the cell envelope (3). The question mark indicates an unresolved aspect of the anchoring mechanism.

associated with the *P. aeruginosa* T6SS[45] (Supplementary Fig. 13d). These results suggest that SalCIS encodes two toxic effectors, with SalCgo1 utilising an unknown mechanism of action, although we cannot rule out that the effect of SalCgo1 overexpression is non-specific and due to its non-native expression levels. We were unable to conclusively prove that the toxicity of these effectors is caused by the HEXXH motif. Notably, studies of the AlgoCIS effectors Cgo1 and Cgo2 demonstrated how both exhibited toxicity and similar HEXXH motifs[4], which the authors were unable to abolish upon mutation of the motif. Several other EATS studies have also reported the HEXXH motif [42,43].

SalCIS represents a distinct cluster of CISs

Based on the membrane-associated structure of SalCis20, the predicted trimeric architecture of SalCis13, and the extended domain IV of SalCis11, we searched for related CIS operons containing homologues of these components. This analysis identified a distinct group of CISs that share conserved features, and are distinct from eCIS and T6SSs (Fig. 6a, Supplementary Fig. 14 and Supplementary Data 2). Specifically, they lack membrane-bound baseplate homologues of T6SS baseplate components, and do not have variable regions as T6SSs do. Compared to eCISs, SalCIS and similar systems also exhibit operon arrangements that differ from canonical eCISs (Supplementary Fig. 14). Phylogenetic comparison of their sheath proteins revealed a coherent cluster, suggesting evolutionary and functional relatedness (Fig. 6b). All operons in this cluster also encode a homologue of SalCgo2, perhaps a core effector of this CIS subtype. Notably, SalCgo1 homologues are absent from most of these CIS clusters, including canonical eCIS and T6SS, and therefore SalCgo1 may be a lineage-specific toxin acquired horizontally by *S. enterica* and *P. polaris*. Protein-protein interaction modelling employing AlphaPulldown[46] of all proteins in the

operon versus each other revealed predicted interactions supporting our models (Supplementary Fig. 15). Taken together, we hypothesise that SalCIS belongs to a structurally distinct subtype of CISs, potentially specialised for inner membrane association (Fig. 6c).

In this study, we present the near-complete atomic structure of, to the best of our knowledge, a previously uncharacterised extracellular contractile injection system (SalCIS) in *Salmonella enterica* subsp. *salamae*. Our data suggest that the SalCIS shares some core structural architecture and contractile mechanism typical of CISs, including the contractile sheath, inner tube, baseplate and spike, as in eCISs, yet exhibits significant deviation from canonical eCIS and T6SS architecture. Saliently, unlike PVCs and Afp, SalCIS appears to operate as a membrane-associated complex. We did not detect extracellular secretion or release of structural components or toxins, but this is likely because the activation conditions remain unknown.

Central to this divergence is the presence of an integral membrane protein, with a putative hydrolase domain, and the Afp13-like SalCis13, within the core SalCIS operon. These proteins were structurally predicted to interface with the baseplate, suggesting a model in which SalCIS interacts with the inner membrane, rather than being released extracellularly. Cryo-ET analyses further support this membrane association, as we observed long SalCIS assemblies perpendicular to the inner membrane surface, though we could not definitively resolve anchoring orientation due to cell thickness.

We identified two putative effectors within the operon, SalCgo1 and SalCgo2. SalCgo2 exhibits mild periplasmic toxicity, while SalCgo1 was toxic in both periplasmic and cytosolic contexts in *E. coli*, suggesting a distinct but incompletely characterised mode of action. The mutation of the HEXXH motif did not abolish toxicity in SalCgo1, perhaps pointing to a multi-motif toxin mode of action, wherein the HEXXH motif works in tandem with a thus far uncharacterised toxic fold. Furthermore, at this point, it cannot be completely ruled out that the observed toxicity is related to the overexpression of SalCgo1, at least in our experiment in a heterologous system. The presence of these putative effectors underscores the potential of SalCIS as a functionally active system, likely regulated in contexts beyond the tested conditions.

Our findings pose SalCIS as an emerging class of CISs that appear domesticated, conditionally regulated for niche-specific interactions, such as competition or symbiosis. The large structural size of SalCIS and its membrane interaction offer promising avenues for future bioengineering efforts to deliver customised effectors in targeted drug delivery applications.

Methods

SalCIS plasmids and mutant strains

The entire SalCIS operon was cloned from *Salmonella enterica* subsp. *Salamae* serovar Greenside strain NCTC9936. The operon was cloned as on the genome, except SalCis15, SalCgo1 and SalCgo2 were reversed. Genomic DNA was purified with the Nanobind CBB big DNA kit (Circulomic). Gene fragments were PCR-amplified, using commercially sourced primers (TAG Copenhagen, see Source Data file for sequences) and cloned into linearised pBAD33 by In-Fusion cloning (Takara Bio). Deletions of SalCis16b, SalCis13 and SalCis20 were generated by PCR and In-Fusion assembly. SalCis20 was cloned similarly (homemade LIC, IPTG inducible plasmid, kanamycin resistance, C-terminal single non-cleavable Strep-tag II). For spot assays, SalCgo1 and SalCgo2 mutants, and fusion plasmids were produced by gene synthesis and sub-cloning on pET-11a (GenScript). For single particle analysis, CIS plasmids were electroporated into electrocompetent BL21 Star™ (DE3) cells (2.5 kV, 25 mF, 200 Ω). For cryo-ET, CIS plasmids were transformed into electrocompetent *S.* Typhimurium mutant strains. Mini-cell *S.* Typhimurium mutants were generated with the λ Red system by deleting *minD* in a BSL-1 strain. Deletion of SalCIS from the *S. enterica* subspecies *salamae* genome was also performed using λ Red, in parts (Supplementary Table 4). Plasmids were verified by whole plasmid nanopore sequencing (Macrogen Europe).

SalCIS heterologous expression

For single particle cryo-EM, SalCIS or mutants were expressed in *E. coli* BL21 Star™ (DE3) in 2 L of LB medium, with appropriate antibiotics (100 μg mL^{-1} ampicillin and / or 34 μg mL^{-1} chloramphenicol, 37 °C, 180 r.p.m), grown to OD_{600} 0.8. Expression was induced (0.2% w/v L-arabinose and/or 0.5 mM IPTG), incubation continued at 37 °C, to OD_{600} 1.2, then cooled (18 °C, 70 r.p.m, 24 h). For cryo-ET, *S.* Typhimurium harbouring SalCIS plasmids were grown to OD_{600} 0.2 (37 °C, 180 r.p.m), induced (0.2% w/v L-arabinose), to OD_{600} 0.8, cooled to 18 °C, induced again, and grown (24 h, 70 r.p.m). For membrane-bound SalCis20, 2 L of *E. coli* BL21-Gold™ cells harbouring the SalCis20 plasmid were grown to OD_{600} 1.0 at 37 °C in Terrific Broth, and induced (0.5 mM IPTG, 24 h, 16 °C, 180 r.p.m), pelleted (5000 *g*, 20 min), and flash frozen.

SalCIS purification

E. coli BL21 Star™ (DE3) cells with SalCIS expression induced were pelleted (5000 *g*, 15 min), resuspended in 100 mL cold Milli-Q water, and pelleted again (5000 *g*, 15 min). Pellets were flash-frozen, thawed, resuspended (20 mL lysis buffer: 50 mM Tris-HCl, 150 mM NaCl, 1% Triton X-100, 0.5x CellLytic Reagent (Sigma-Aldrich), 200 μg mL^{-1} lysozyme (in 10 mM Tris-HCl, pH 8.5), 50 μg mL^{-1} DNase I, 5 mM EDTA, 10 mM $MgCl_2$, protease inhibitor cocktail (Roche), pH 7.4) and incubated at 37 °C for 30 min. Debris was cleared (15,000 *g*, 15 min), then clarified (30,000 *g*, 30 min). Supernatant was spun to pellet CIS (100,000 *g*, 1 hr). Pellets were resuspended (1 mL, resuspension (RS) buffer: 50 mM Tris-HCl, 150 mM NaCl, protease inhibitor cocktail (Roche), pH 7.4), by gentle rolling (4 °C, 1 h), loaded on a 10–40% iodixanol gradient, in RS buffer and centrifuged (100,000 *g*, 24 h). Fractions were analysed by SDS-PAGE and Western Blot, pooled and dialysed (4 °C, 4 days) to remove iodixanol, pelleted (100,000 *g*, 1 h), and used for negative stain TEM and cryo-EM. For LC-MS/MS, the bidirectional operon was co-expressed (SalCis16a-SalCis20 on pBAD33 and SalCis15-SalCgo1 on pET-11a), and purified identically.

SalCIS membrane component purification

Pellets were thawed and resuspended in lysis buffer (20 mM Tris-HCl, 150 mM NaCl, 10 mM $MgCl_2$, 5 mM EDTA, 1 mM TCEP, and 10% glycerol, pH 7.5). Homogenised (10 °C, 2 h) cells were lysed twice with an Avestin Emulsiflex C5. Debris was removed (10,000 *g*, 15 min). Membranes were pelleted (30,000 *g*, 1 h), and solubilized overnight (10 °C, stirring) with 1% Lauryl maltose neopentyl glycol (LMNG). Insoluble material was removed (100,000 *g*, 1 h), SalCis20 was isolated (single Strep-II tag, gravity drop), eluted, and further purified using size exclusion chromatography (Superdex 200 GL, GE Healthcare) equilibrated in buffer with 0.002% LMNG. SalCis20 eluted at 300 kDa and was used for SDS-PAGE, Western blot analysis and cryo-EM grids.

To isolate SalCIS from endogenous expression, *S. enterica* subspecies *salamae* harbouring plasmid-borne wildtype SalCIS were induced (0.2% v/v L-arabinose) at OD_{600} 1.0 (60 rpm, 18 °C, 24 h), pelleted (6000 *g*, 20 min), flash frozen, thawed, resuspended (20 mM Tris-HCl, 150 mM NaCl, 10 mM $MgCl_2$, 5 mM EDTA, 1 mM TCEP, and 10% glycerol, pH 7.5). Cells were sonicated (30% amplitude, 15 s on/20 s off pulses, 10 min on ice), debris pelleted (13,000 *g*, 20 min), and homogenised (40 Dounce passes). Membranes were pelleted (100,000 *g*, 1 h), solubilized (1% DDM, 4 °C, 24 h). Membrane and CIS were pelleted through a 40% (150,000 *g*, 1 h), resuspended, cleaned on a 10-40% sucrose gradient, fractionated, and examined by TEM and Western blot (Supplementary Fig. 13a).

Negative-stain TEM

Concentrated CIS were cleared (10,000 *g*, 20 min). Samples (4 μL) were applied to glow-discharged (15 mA, 45 s), continuous-carbon Cu

grids (200 mesh) for 60 s, washed twice with RS buffer, stained with 2% uranyl acetate (60 s) and imaged on a Morgagni TEM (Thermo Fisher Scientific) at 80 kV.

Single particle cryo-EM

SalCIS ΔSalCis13-ΔSalCis20 mutant (3.5 µL) was applied to glow-discharged (5 mA, 10 s) R2/2 200 mesh (Quantifoil) Cu grids, coated with 2 nm continuous Carbon, blotted (blot force −8, 3 s), and plunge-frozen in liquid ethane (Vitrobot™ Mark IV). Purified SalCis20 (2.5 mg mL^{-1}) was applied to glow-discharged (15 mA, 30 s) R0.6/1 200 mesh (Quantifoil) Au grids, blotted (blot force 15, 5 s) and vitrified. SalCIS full operon (3.5 µL) was applied to glow-discharged (5 mA, 10 s) R2/2 300 mesh (Quantifoil) Cu grids, coated with 2 nm continuous Carbon, and blotted the same way. For SalCIS ΔSalCis13-ΔSalCis20, data were collected on a Titan Krios G2 (Thermo Fisher Scientific), at 300 kV, with a Selectris X energy filter (10 eV slit) and Falcon 4i detector, magnification 165,000 (pixel size 0.728 Å), defocus 0.5–2.5 µm, total dose of 42 e^- $Å^2$ fractionated into 40 frames (EPU). For SalCis20, data were collected in an identical fashion with a total dose of 54 e^- $Å^2$, fractionated into 40 frames (EPU), however due to a slight orientation bias, we additionally collected tilted data at −40° and +40°. For SalCIS, full operon data were collected on a Glacios (Thermo Fisher Scientific), at 200 kV, Falcon 3 detector, magnification 92,000 (pixel size 1.6 Å), defocus 0.8–3.0 µm, total dose 40 e^- $Å^2$ fractionated into 40 frames (EPU).

Single particle cryo-EM processing

All image analysis and reconstructions were done in cryoSPARC[47] (Supplementary Fig. 16). ~80,000 movies were patch motion-corrected, and CTF estimated, blob-picked particles were curated, bad particles removed, then 2D-classified. Baseplates, caps and extended sheath assemblies were picked, selected 2D classes seeded as template picking and further 2D classification. Initial reconstructions (C6) were followed by 3D classification and manual inspection. For the cap, 700 particles were picked manually, and an initial reconstruction (C6) generated 2D templates for template picking. Chosen volumes and underwent homogenous refinement (C6), re-extraction with per particle CTF, reconstruction-only, homogenous refinement, and a final non-uniform refinement (C6 and C3), yielding maps (global resolution 3.0 Å) (Supplementary Table 4). Symmetry-expanded local refinements produced baseplate (C6), cap (C6), central spike (C3), and extended sheath (helical, C6), resulting in maps at a resolution of 2.86 Å and 2.97 Å, and 2.3 Å, respectively (Supplementary Figs. 16, 17). A contracted sheath dataset (8060 movies) processed similarly, yielded a 3.24 Å map (helical, C6, Supplementary Fig. 18). A ~ 42067 movies dataset of SalCis20, processed similarly (C2), yielded a 2.73 Å resolution map (Supplementary Figs. 16, 17).

Atomic model building

AlphaFold2-multimer models (Supplementary Fig. 19) were rigid-body fit into maps in ChimeraX[48] and refined with ISOLDE[49], and manually rebuilt. Two maps (non-sharpened, non-uniform, C6) were used for C6 baseplate components (SalCis11, SalCis12, SalCis2, and SalCis9) to compensate for missing densities after superimposition of maps. Broken down map edge densities required two masked local refinements. Masks were generated with Segger[50]. SalCis10, SalCis8, SalCis6, SalCis7 and SalCis5, AlphaFold2 predicted, and built onto the baseplate spike puncture complex map. Two cap densities fitted AlphaFold2 predicted models of SalCis16a, SalCis16b, and terminal sheath/inner-tube segments. The extended sheath map guided fitting of AlphaFold2-multimer models of SalCis2 and SalCis1, followed by similar fitting, building and refinement. SalCis2 was built into the contracted sheath map and rebuilt similarly. All models underwent iterative PHENIX[51] real-space refinement (Supplementary Fig. 20). Unresolved predicted segments were truncated (Supplementary Table 1.). Validation used MolProbity[52] (PHENIX) (Supplementary Table 5). Figures were prepared in ChimeraX.

Cryo-ET sample preparation

S. Typhimurium heterologously expressing *S. enterica* subspecies *salamae* CIS were pelleted (2000 *g*, 20 min), resuspended in cell resuspension (CRS) buffer (136 mM NaCl, 2.5 mM KCl, 1.3 mM $MgCl^2$, 2 mM $CaCl^2$, 10 mM HEPES, 10 mM D-glucose, sterile filtered), and incubated (ambient temperature, 1 h). A sample (2.5 µL) was applied to glow-discharged (15 mA, 45 s) Quantifoil R2/2 Au 200 mesh (Jena Bioscience) grids. Protein-A 10 nm Gold Conjugate (0.5 µL, Cytodiagnostics) was mixed into the drop, incubated (1 min) manually back blotted (9 s), plunge frozen (Vitrobot Mark IV), and stored in liquid nitrogen.

Cryo-ET data collection

Two datasets were acquired. First: Titan Krios G2, 300 kV, FEG, Ceta-D camera and a Gatan K3 BioQuantum detector, with SerialEM, pixel size 2.16 Å, dose symmetric, 2 ° increments, −58 ° to +58 °, defocus −10 to −3 µm, total accumulated dose of 110 −120 e^- $Å^{-2}$ (SciLifeLab, Stockholm). Second: Titan Krios G3i (I), BioQuantum LS imaging filters (slit width 20 eV) and a Gatan K3 detector, employing Tomo5 automated acquisition, low-magnification search maps set anchor points, 2° or 3° increments, −60° to +60°, defocus of −9 to −7 µm, total 130 – 150 e^- $Å^{-2}$, and a pixel size of 2.182 Å (Diamond Light Source, Oxfordshire).

Tomogram reconstruction and segmentation

Cryo-electron tomograms were processed with IMOD[53]. Fiducial-based alignment was carried out, CTF corrected (Ctfplotter), and reconstructed using weighted back-projection, with an SIRT-like filter (12). Tomograms were visualised and manually annotated in 3Dmod. SalCIS bundles were segmented as tubes[54]: open contours along the central axis of each SalCIS particle were interpolated, and a surface was generated. Membranes were segmented with MemBrain[55]. Models were imported into ChimeraX for annotation, visualisation, and figure generation; SalCIS bundles, membranes, and vesicles were coloured.

Epifluorescence microscopy

T7 polymerase-expressing *S.* Typhimurium transformed with SalCis20-mKate2, or mutant, were grown in LB (50 µg mL^{-1} kanamycin, 37 °C, 24 h, 180 r.p.m). Cultures were diluted 1:100 into 10 mL LB (50 µg mL^{-1} kanamycin, 0.4% w/v D-glucose), incubated (37 °C, 180 r.p.m) to the exponential phase. Non-induced samples were adjusted to an OD_{600} of 0.2 in LB (0.4% g w/v D-glucose) applied to 1% agarose pads (PBS), and imaged. Remaining cells were washed twice in LB (14,000 *g*, 5 min), resuspended in LB (50 µg mL^{-1} kanamycin), and induced (0.1 mM IPTG, 37 °C, 180 r.p.m, ~2 h). Samples were adjusted to an OD_{600} of 0.2 in LB, applied to 1% agarose pads (PBS), and imaged. Imaging used a Nikon Eclipse Ti2 inverted epifluorescence microscope with a Fusion BT camera and a CFI Plan Apochromat DM 60 × Lambda Oil Ph3/1.40 objective. Acquisition (16-bit) used a 1.5 µm *Z*-range (0.3 µm steps), 594 nm laser at 30% intensity, 500 ms exposure, Tri-Band CFP/YFP/mCherry turret filter, plus emission filter FF01-680/42 (Semrock), in an MXR00765 Sedat Penta wheel (DAPI/FITC/TRITC/Cy5/Cy7) was used. Z-stacks were acquired, and middle-plane phase-contrast images are shown (Fig. 5a, b). Intensity profiles were extracted in Fiji/ImageJ (v2.16) by drawing straight lines perpendicular to the long axis of isolated cells; one-dimensional profiles (x_i, y_i) were exported and mean ± SD were calculated and visualised in GraphPad Prism version 10.0.0, GraphPad Software, Boston, Massachusetts USA, www.graphpad.com (Source Data Fig. 5a, b, Supplementary Note 2, and Fig. 5a, b).

Secretion assays and Western blotting

S. enterica subspecies *salamae* with (ΔSalCIS) and without deletion of SalCIS were transformed with SalCIS genes. ORFs 1–15 (SalCis16a-

SalCis20) were on pBAD33 (L-arabinose inducible); ORFs 16–18 (SalCis15-SalCgo1) were on pWSK29 (Tet-inducible). Strain and controls were cultured in LB (100 μg mL^{-1} ampicillin and / or 34 μg mL^{-1} chloramphenicol, 37 °C, 180 r.p.m). Overnight cultures were diluted 1:100 into 15 mL LB and grown (1 h), and induced (0.2% w/v L-arabinose and / or 100 ng mL^{-1} anhydrous tetracycline, 2.5 h). A 1.9 mL aliquot was harvested; cells and supernatant separated (13,000 *g*, 3 min). Supernatant (1 mL) proteins were precipitated with 10% (v/v) trichloroacetic acid (TCA) (30 min, on ice), pelleted (20,000 *g*, 30 min, 4 °C), air-dried, and resuspended in 2 × SDS sample buffer. Cellular and supernatant fractions were normalised to 20 OD units μL^{-1}, resolved by SDS-PAGE, and transferred to nitrocellulose membranes for Western blotting. Detection used custom polyclonal antibodies: anti-SalCis2 (0.2 μg mL^{-1}), -SalCis1 (1.5 μg mL^{-1}), -SalCgo1 (0.1 μg mL^{-1}), and -SalCgo2 (0.2 μg mL^{-1}). Cytosolic contamination was assessed by anti-DnaK (0.1 μg mL^{-1}).

LC-MS/MS data generation and analysis

Purified SalCIS (100 μg) was diluted in 200 μL 50 mM TRIS pH 8.5 and split into two equal aliquots. Each was processed by either in-solution digestion or Protein Aggregation Capture (PAC). Digestion employed sequencing-grade trypsin (Promega) or endoproteinase Lys-C (Wako). For in-solution digestion, 0.25 μg enzyme was added, and samples were incubated overnight at 25 °C. For PAC, proteins were precipitated with 10 volumes of acetonitrile and immobilised on magnetic microparticles. Microparticles were fixed on a magnet stand, washed twice with 100% acetonitrile and once with 70% ethanol, air-dried (15 min), and resuspended (50 mL, 50 mM TRIS, pH 8.5). Digestion employed 0.25 μg enzyme and incubated (overnight, 30 °C, 1250 r.p.m). Microparticles were refixed, and digests were transferred to new tubes. In both workflows, reduction and alkylation were performed by adding tris (2-carboxyethyl) phosphine and chloroacetamide (10 mM), and incubated (30 °C, 30 min). Samples were clarified through 0.45 μm spin filters, and peptides were purified on low-pH C18 StageTips. StageTips were prepared in-house, with four plugs of C18 material (Sigma-Aldrich, Empore SPE Discs, C18, 47 mm). Tips were activated with 100 μL 100% methanol, equilibrated with 100 μL 80% acetonitrile (ACN) in 0.1% formic acid (FA), and washed twice with 100 μL 0.1% FA. Samples were acidified (1% v/v trifluoroacetic acid, pH < 3.0), loaded, washed twice with 0.1% FA, and eluted using 80 μL 25% ACN in 0.1% FA. Eluates were dried in a SpeedVac at 60 °C, re-dissolved in 20 μL 0.1% FA and stored at −20 °C until LC-MS/MS.

The digests were analysed on a Vanquish™ Neo UHPLC system (Thermo) coupled to an Orbitrap™ Astral™ mass spectrometer (Thermo), in triplicate injections (1, 2, and 3 μL). Analysis employed analytical columns (15 cm, 75 μm ID, packed in-house with ReproSil-Pur 120 C18-AQ 1.9 μm beads (Dr. Maisch)). Peptides were eluted at 250 nL min^{-1} from buffer A (0.1% FA) to buffer B (80% acetonitrile in 0.1% FA), using a 30 min Gradient (20 min analytical, 5–38% B). The column was held at 45 °C, ionisation used a NanoSpray Flex™ NG source, 2 kV spray voltage, 275 °C ion-transfer tube, and an RF lens 50%. MS1 scans were acquired using the Orbitrap™, MS2 in the Astral™. MS1: 300–1300 *m/z*, resolution 120,000, AGC 2.5×10^6, injection 150 ms. Data-dependent acquisition (DDA) selected charges 2-6, isolation 1.3 *m/z*, and fragmented using higher-energy collision dissociation (HCD) with normalised collision energy of 25. Monoisotopic Precursor Selection (MIPS) "Peptide" mode was enabled. Dynamic exclusions: 7.5 s, 10 ppm tolerance, expected peak-width 10 s, isotopes excluded. MS2: 100–1500 *m/z*, AGC 2.5×10^4, intensity ≥1 ×nm 10^5 charges per second, injection 5 ms.

MS RAW data were analysed in MaxQuant (v.2.4.3.0). All files were searched together, with default settings, unless stated. Theoretical spectra were generated from in-silico digestion of 18 SalCIS proteins; the MaxQuant contaminant database was included. Digestion used trypsin/P or Lys-C/P (semi-specific), peptide length 6-55. Carbamidomethylation of cysteine was fixed. Variable modifications: oxidation (methionine), N-terminal acetylation, deamidation (Glutamine/Asparagine), and pyroglutamate conversion, with a maximum of 3 per peptide. Peptides required score ≥100, and delta score ≥50. The second peptide search was disabled. Label-free quantification (LFQ) was enabled, with "Fast LFQ" disabled. MaxQuant 1% FDR filtering was applied at the PSM and protein levels.

For extended analysis, four additional data searches were performed. In all, N-terminal acetylation was disabled (absent in prokaryotes). The initial search only differed here. The second used full digestion up to three missed cleavages for the trypsin, and two for Lys-C. The third included *E.coli* reference proteome (ECOLI_UP000000625, Uniprot on the 12th, August 2025; 4414 entries). The fourth combined fully specific digestion and the *E. coli* reference proteome. Supplementary Table 2 lists search statistics; interpretation and visualisation derived solely from initial analysis.

SDS-PAGE and Western blotting

Samples were diluted and denatured (1:6, 5 min, 95 °C) in Laemmli buffer (Thermo Fisher Scientific), loaded on 4–12% Bis-Tris precast gels (Thermo Fisher Scientific) and run at 200 V in 1 × MES, for 35 min. Gels were Coomassie-stained. For Westerns, gels were transferred to nitrocellulose (iBlot 2, Transfer Stacks, Invitrogen) using the iBlot system (20 V, 6 min). Membranes underwent sequential lateral flow (SLF), were blocked with iBind kit (Invitrogen), incubated with primary and secondary antibodies (1:1000, 3 h–overnight), and developed with TMB-D blotting solution (Kementec).

Toxicity assays

S. enterica CIS effectors were cloned into pET-11a; The *OmpA* periplasmic signal sequence was fused to the effector and mutant N-termini, individually and in tandem. Controls included non-fusion effectors, *Pseudomonas aeruginosa* Tse1 / 2, and sfGFP-*OmpA* fusions. Motif and point mutants (HEXXH and point mutants) were generated by PCR. Plasmids were transformed into chemically competent *E. coli* BL21™ (DE3) pLysS by heat shock (42 °C, 45 s). Overnight cultures were grown in LB medium (100 μg mL^{-1} ampicillin, 34 μg mL^{-1}, 1% w/v D-glucose, 20 h). Cultures were normalised to OD_{600} 0.8, pelleted (6000 *g*), resuspended in fresh LB, serially diluted, and spotted on plates under induction (0.5 mM IPTG) and suppression (1% w/v D-glucose) conditions. Plates were incubated (37 °C, 24 h) and imaged.

Bioinformatic analysis

The operon was identified employing the eCIS-screen script[1]; operon boundaries were confirmed by Shine-Dalgarno sequences (AGGAGG and GAGG). HHPred (MPI Toolkit) assessed sequence-based structural homology[56]. AlphaFold2-Multimer predicted structures of all SalCIS proteins[57]. Predicted models were queried on the DALI server for structural homologues[58]. Transmembrane helices were predicted with the DeepTMHMM 1.0 server[59]. Signal peptides were predicted with SignalP 6.0[30]. Operon alignment and gene-cluster visualisation used Clinker[60]. Electrostatics were computed with the Adaptive Poisson–Boltzmann Solver (APBS) at pH 7.4, (default dielectric)[61]. All-vs-all AlphaFold3 predictions and plotting were carried out using custom scripts (Supplementary Figs. 8b, 15). All-vs-all analysis used 5 models, at 5 random seeds, creating 25 models for analysis; heatmap values are the mean average of those scores. Multiple sequence alignment visualisation used ESPript 3.0[62]. Heat maps were generated using R (v.2023.12.1 + 402) using RStudio (Posit).

Statistics and reproducibility

No statistical method was used to determine any sample size. No data were excluded from the analyses. The experiments were not randomised. The investigators were not blinded to allocation during

experiments and outcome assessment. Representative negative-stain TEM micrographs and fluorescence microscopy images shown are from experiments repeated as indicated in the figure legends. Intensity profiles in Fig. 5a, b were derived from ±SD of $n = 21$ cells, and ±SD of $n = 20$ cells, respectively. Error bars represent SD, as stated in the figure legend. Cryo-EM data were collected from single preparations; the quality and resolution of reconstructions were assessed by gold-standard Fourier shell correlation (FSC = 0.143 criterion), as reported in Supplementary Table 5.

Reporting summary

Further information on research design is available in the Nature Portfolio Reporting Summary linked to this article.

Data availability

The atomic coordinates and cryo-EM density maps have been deposited in the PDB and EMDB. The accession numbers are listed as follows: PDB 9RCE (Baseplate module in extended state); EMD-53919 (baseplate reconstructed in C3 symmetry); PDB 9R9N (cap module in extended state); EMD-53859 (cap reconstructed in C6 symmetry); PDB 9R9H (sheath and inner tube module in extended state); EMD-53857 (extended sheath and inner tube reconstructed in C6 symmetry); PDB 9R9I (sheath in contracted state); EMD-53858 (sheath, contracted reconstructed in C6 symmetry); PDB 9R9A (a membrane protein, SalCis20 as a dimer in LMNG); EMD-53855 (membrane protein SalCis20 reconstructed in C2 symmetry). The raw cryo-EM data have been deposited in the EMPIAR database, EMPIAR-13089 (SalCIS-ΔSalCis13-ΔSalCis20 mutant); EMPIAR-13088 (SalCIS Wt); EMPIAR-13087 (membrane protein, SalCis20). The mass spectrometry proteomics data have been deposited to the ProteomeXchange Consortium via the PRIDE[63] partner repository with the dataset identifier PXD063506 (full SalCIS operon). Source data underlying all graphs and plots (including Fig. 5a, b and Supplementary Figs.) are provided as a Source Data file with this paper. Protein sequence alignments of SalCgo1 and SalCgo2 are provided in Supplementary Data 1. Genetic operons used to generate synteny analysis figures (Fig. 6a and Supplementary Fig. 14) are provided in Supplementary Data 2. Source data are provided with this paper.

Code availability

The in-house scripts used for All-vs-all AlphaFold3 predictions are available at Github [https://github.com/FJ0M/SalCIS_AF3_allvall] and Zenodo [https://doi.org/10.5281/zenodo.18881441][64].

References

1. Chen, L. et al. Genome-wide Identification And Characterization Of A Superfamily Of Bacterial Extracellular Contractile Injection Systems. *Cell Rep* **29**, 511–521.e2 (2019).
2. Lin, L. The expanding universe of contractile injection systems in bacteria. *Curr. Opin. Microbiol.* **79**, 102465 (2024).
3. Weiss, G. L. et al. Structure of a thylakoid-anchored contractile injection system in multicellular cyanobacteria. *Nat. Microbiol.* **7**, 386–396 (2022).
4. Xu, J. et al. Identification and structure of an extracellular contractile injection system from the marine bacterium Algoriphagus machipongonensis. *Nat. Microbiol.* **7**, 397–410 (2022).
5. Jiang, F. et al. Cryo-EM structure and assembly of an extracellular contractile injection system. *Cell* **177**, 370–383.e15 (2019).
6. Taylor, N. M. I., Van Raaij, M. J. & Leiman, P. G. Contractile injection systems of bacteriophages and related systems. *Mol. Microbiol.* **108**, 6–15 (2018).
7. Kikuchi, Y. & King, J. Genetic control of bacteriophage T4 baseplate morphogenesis. *J. Mol. Biol.* **99**, 645–672 (1975).
8. Taylor, N. M. I. et al. Structure of the T4 baseplate and its function in triggering sheath contraction. *Nature* **533**, 346–352 (2016).
9. Heymann, J. B. et al. Three-dimensional structure of the toxin-delivery particle antifeeding prophage of Serratia entomophila. *J. Biol. Chem.* **288**, 25276–25284 (2013).
10. Evans, R. & Waterfield, N. R. The Pvc15 ATPase selectively associates effector proteins with the *Photorhabdus* virulence cassette. *R. Soc. Open Sci.* **11**, 240948 (2024).
11. Heiman, C. M., Vacheron, J. & Keel, C. Evolutionary and ecological role of extracellular contractile injection systems: from threat to weapon. *Front. Microbiol.* **14**, 1264877 (2023).
12. Kreitz, J. et al. Programmable protein delivery with a bacterial contractile injection system. *Nature* **616**, 357–364 (2023).
13. Vlisidou, I. et al. The Photorhabdus asymbiotica virulence cassettes deliver protein effectors directly into target eukaryotic cells. *eLife* **8**, e46259 (2019).
14. Steiner-Rebrova, E. M. *et al*. N-terminal toxin signal peptides efficiently load therapeutics into a natural nano-injection system. Preprint at *bioRxiv* https://doi.org/10.1101/2023.11.13.566157 (2023).
15. Bhardwaj, P., Mitra, A. K. & Hurst, M. R. H. Investigating the process of sheath maturation in antifeeding prophage: a phage tail-like protein translocation structure. *J. Bacteriol.* **203**, e0010421 (2021).
16. Desfosses, A. et al. Atomic structures of an entire contractile injection system in both the extended and contracted states. *Nat. Microbiol.* **4**, 1885–1894 (2019).
17. Böck, D. et al. In situ architecture, function, and evolution of a contractile injection system. *Science* **357**, 713–717 (2017).
18. Casu, B., Sallmen, J. W., Schlimpert, S. & Pilhofer, M. Cytoplasmic contractile injection systems mediate cell death in Streptomyces. *Nat. Microbiol.* **8**, 711–726 (2023).
19. Ho, B. T., Dong, T. G. & Mekalanos, J. J. A view to a kill: the bacterial type vi secretion system. *Cell Host Microbe* **15**, 9–21 (2014).
20. Bleumink-Pluym, N. M. C., Van Alphen, L. B., Bouwman, L. I., Wösten, M. M. S. M. & Van Putten, J. P. M. Identification of a functional type VI secretion system in campylobacter jejuni conferring capsule polysaccharide sensitive cytotoxicity. *PLoS Pathog* **9**, e1003393 (2013).
21. Mougous, J. D. et al. A virulence locus of *Pseudomonas aeruginosa* encodes a protein secretion apparatus. *Science* **312**, 1526–1530 (2006).
22. Billah, M. M. & Rahman, M. S. Salmonella in the environment: a review on ecology, antimicrobial resistance, seafood contaminations, and human health implications. *J. Hazard. Mater. Adv.* **13**, 100407 (2024).
23. Ofori, L. A. et al. Salmonella enterica in farm environments in the Ashanti Region of Ghana. *BMC Microbiol* **23**, 370 (2023).
24. Parsons, S. K., Bull, C. M. & Gordon, D. M. Spatial variation and survival of salmonella enterica subspecies in a population of Australian sleepy lizards (Tiliqua rugosa). *Appl. Environ. Microbiol.* **81**, 5804–5811 (2015).
25. Yan, M. et al. *Salmonella enterica* subsp. II serovar 4,5,12:a:- may cause gastroenteritis infections in humans. *Gut Microbes* **14**, 2089007 (2022).
26. Lien, Y.-W. et al. Mechanism of bacterial predation via ixotrophy. *Science* **386**, eadp0614 (2024).
27. Shneider, M. M. et al. PAAR-repeat proteins sharpen and diversify the type VI secretion system spike. *Nature* **500**, 350–353 (2013).
28. Yap, M. L. & Rossmann, M. G. Structure and function of bacteriophage T4. *Future Microbiol* **9**, 1319–1327 (2014).
29. Beveridge, T. J. Structures of gram-negative cell walls and their derived membrane vesicles. *J. Bacteriol.* **181**, 4725–4733 (1999).
30. Nielsen, H., Teufel, F., Brunak, S. & Von Heijne, G. SignalP: the evolution of a web server. in *Protein Bioinformatics*. (ed. Lisacek, F.) **2836**, 331–367 (Springer US, New York, NY, 2024).
31. Pradel, N., Delmas, J., Wu, L. F., Santini, C. L. & Bonnet, R. Sec- and tat-dependent translocation of β-lactamases across the *Escherichia*

coli inner membrane. *Antimicrob. Agents Chemother.* **53**, 242–248 (2009).
32. Üstok, F. I., Chirgadze, D. Y. & Christie, G. Structural and functional analysis of SleL, a peptidoglycan lysin involved in germination of *B acillus* spores: crystal structures for the bacillus spore lytic enzyme sleL. *Proteins Struct. Funct. Bioinforma.* **83**, 1787–1799 (2015).
33. Tidhar, A., Rushing, M. D., Kim, B. & Slauch, J. M. Periplasmic superoxide dismutase SODCI of *s almonella* binds peptidoglycan to remain tethered within the periplasm. *Mol. Microbiol.* **97**, 832–843 (2015).
34. Byun, B. et al. Mechanism of the Escherichia coli MltE lytic transglycosylase, the cell-wall-penetrating enzyme for Type VI secretion system assembly. *Sci. Rep.* **8**, 4110 (2018).
35. Ashkenazy, H. et al. ConSurf 2016: an improved methodology to estimate and visualize evolutionary conservation in macromolecules. *Nucleic Acids Res* **44**, W344–W350 (2016).
36. English, G. et al. New secreted toxins and immunity proteins encoded within the T ype VI secretion system gene cluster of *s erratia marcescens*. *Mol. Microbiol.* **86**, 921–936 (2012).
37. Sibinelli-Sousa, S. et al. A family of T6SS antibacterial effectors related to l,d-transpeptidases targets the peptidoglycan. *Cell Rep* **31**, 107813 (2020).
38. Monchois, V., Abergel, C., Sturgis, J., Jeudy, S. & Claverie, J.-M. Escherichia coli ykfE ORFan gene encodes a potent inhibitor of C-type lysozyme. *J. Biol. Chem.* **276**, 18437–18441 (2001).
39. Rapisarda, C. et al. In situ and high-resolution cryo- EM structure of a bacterial type VI secretion system membrane complex. *EMBO J.* **38**, e100886 (2019).
40. Caulton, S. G. et al. Bdellovibrio bacteriovorus uses chimeric fibre proteins to recognize and invade a broad range of bacterial hosts. *Nat. Microbiol.* **9**, 214–227 (2024).
41. Wood, T. E. et al. The Pseudomonas aeruginosa T6SS delivers a periplasmic toxin that disrupts bacterial cell morphology. *Cell Rep* **29**, 187–201.e7 (2019).
42. Geller, A. M. et al. The extracellular contractile injection system is enriched in environmental microbes and associates with numerous toxins. *Nat. Commun.* **12**, 3743 (2021).
43. Danov, A. et al. Identification of novel toxins associated with the extracellular contractile injection system using machine learning. *Mol. Syst. Biol.* **20**, 859–879 (2024).
44. Karyolaimos, A. & de Gier, J.-W. Strategies to Enhance periplasmic recombinant protein production yields in Escherichia coli. *Front. Bioeng. Biotechnol.* **9**, 797334 (2021).
45. Russell, A. B. et al. Type VI secretion delivers bacteriolytic effectors to target cells. *Nature* **475**, 343–347 (2011).
46. Yu, D., Chojnowski, G., Rosenthal, M. & Kosinski, J. AlphaPulldown—a python package for protein–protein interaction screens using AlphaFold-Multimer. *Bioinformatics* **39**, btac749 (2023).
47. Punjani, A., Rubinstein, J. L., Fleet, D. J. & Brubaker, M. A. cryoSPARC: algorithms for rapid unsupervised cryo-EM structure determination. *Nat. Methods* **14**, 290–296 (2017).
48. Pettersen, E. F. et al. UCSF Chimaera—a visualization system for exploratory research and analysis. *J. Comput. Chem.* **25**, 1605–1612 (2004).
49. Croll, T. I. *ISOLDE*: a physically realistic environment for model building into low-resolution electron-density maps. *Acta Crystallogr. Sect. Struct. Biol.* **74**, 519–530 (2018).
50. Pintilie, G. D., Zhang, J., Goddard, T. D., Chiu, W. & Gossard, D. C. Quantitative analysis of cryo-EM density map segmentation by watershed and scale-space filtering, and fitting of structures by alignment to regions. *J. Struct. Biol.* **170**, 427–438 (2010).
51. Afonine, P. V. et al. Towards automated crystallographic structure refinement with *phenix.refine*. *Acta Crystallogr. D Biol. Crystallogr.* **68**, 352–367 (2012).
52. Williams, C. J. et al. MolProbity: More and better reference data for improved all-atom structure validation. *Protein Sci* **27**, 293–315 (2018).
53. Kremer, J. R., Mastronarde, D. N. & McIntosh, J. R. Computer visualization of three-dimensional image data using IMOD. *J. Struct. Biol.* **116**, 71–76 (1996).
54. Noske, A. B., Costin, A. J., Morgan, G. P. & Marsh, B. J. Expedited approaches to whole cell electron tomography and organelle mark-up in situ in high-pressure frozen pancreatic islets. *J. Struct. Biol.* **161**, 298–313 (2008).
55. Lamm, L. et al. MemBrain v2: an end-to-end tool for the analysis of membranes in cryo-electron tomography. Preprint at *bioRxiv* https://doi.org/10.1101/2024.01.05.574336 (2024).
56. Soding, J., Biegert, A. & Lupas, A. N. The HHpred interactive server for protein homology detection and structure prediction. *Nucleic Acids Res.* **33**, W244–W248 (2005).
57. Varadi, M. et al. AlphaFold protein structure database: massively expanding the structural coverage of protein-sequence space with high-accuracy models. *Nucleic Acids Res* **50**, D439–D444 (2022).
58. Holm, L. Dali server: structural unification of protein families. *Nucleic Acids Res* **50**, W210–W215 (2022).
59. Hallgren, J. *et al*. DeepTMHMM predicts alpha and beta transmembrane proteins using deep neural networks. Preprint at *bioRxiv* https://doi.org/10.1101/2022.04.08.487609 (2022).
60. Gilchrist, C. L. M. & Chooi, Y.-H. clinker & clustermap.js: automatic generation of gene cluster comparison figures. *Bioinformatics* **37**, 2473–2475 (2021).
61. Jurrus, E. et al. Improvements to the APBS biomolecular solvation software suite. *Protein Sci* **27**, 112–128 (2018).
62. Gouet, P., Courcelle, E., Stuart, D. I. & M√©toz, F. ESPript: analysis of multiple sequence alignments in PostScript. *Bioinformatics* **15**, 305–308 (1999).
63. Perez-Riverol, Y. et al. The PRIDE database at 20 years: 2025 update. *Nucleic Acids Res* **53**, D543–D553 (2025).
64. Structure of a contractile injection system in *Salmonella enterica* subsp. *salamae*. (2026). FJOM/SalCIS_AF3_allvall: v1 (editorials). *Zenodo* https://doi.org/10.5281/zenodo.18881441.
65. Sievers, F. & Higgins, D. G. Clustal Omega for making accurate alignments of many protein sequences. *Protein Sci.* **27**, 135–145 (2018).

Acknowledgements

The Novo Nordisk Foundation Centre for Protein Research (NNF CPR) is supported financially by the Novo Nordisk Foundation (NNF14CC0001). This work was supported by a grant from the Independent Research Fund Denmark (1030-00289B). We thank the Protein Production Platform at NNF CPR, (especially lab technician Michael Williamson), for their support in cloning large plasmids and the Biophysics Platform at NNF CPR for their support with mass spectrometry analysis; staff at the Core Facility for Integrated Microscopy (especially TEM specialist Michael James Johnson) for their support; Diamond Light Source for time on Krios I, under proposal bi38819, at Harwell United Kingdom, and especially the late Dr. Karen Davies for her support in cryo-ET data collection; Dr. Simon Erlendsson for consultation on cryo-ET sample preparation; Professor Lone Brønsted at Copenhagen University for BSL-2 laboratory support (PHAGE group); Members of the Taylor group, including Nicole Rutbeek for consultation on membrane protein purification; Members of the Kummer and Montoya groups at NNF CPR, and Dr. Magnus Bloch at Birkbeck University of London, for discussions. N.M.I.T. is a member of ISBUC. M.E. acknowledges funding by the Max Planck Society as a Max Planck Fellow.

Author contributions

N.M.I.T and R.N.E conceived the project. C.S.K performed bioinformatic analysis. R.N.E. performed bioinformatic analysis, designed and cloned

primary plasmid constructs, purified proteins and prepared samples. R.N.E performed cryo-EM sample preparation. T.P and N.H.S collected cryo-EM data. R.N.E processed cryo-EM data, reconstructed cryo-EM maps, built, and refined all the structures presented in this study. R.N.E performed cryo-ET sample preparation and collected cryo-ET data with E.M.S.R. R.N.E processed, reconstructed, analysed and annotated tomograms. R.N.E designed and performed toxicity assays. K.F designed and cloned plasmids, performed genetic manipulations, genome editing, secretion assays and subsequent analysis in *S*. Typhimurium and *S. enterica* subspecies *salamae*. K.F. designed and performed light microscopy experiments and interpreted all related data, with M.E. F.J.O.M. performed AlphaFold3 predictions, analysis, bioinformatic analysis and generated figures. I.A.H. designed and performed LC-MS/MS and subsequent analysis, with M.L.N. M.S. prepared and uploaded structures to EMDB and PDB, R.N.E uploaded datasets to EMPIAR. R.N.E. wrote the manuscript and generated figures; all authors commented on the manuscript.

Competing interests

Eva Maria Steiner-Rebrova and Nicholas M. I. Taylor are inventors on a patent application related to eCIS (PCT/EP2023/068102). Eva Maria Steiner-Rebrova is co-founder of Yngvi Bio ApS. The other authors declare no competing interests.

Additional information

Supplementary information The online version contains supplementary material available at https://doi.org/10.1038/s41467-026-71989-6.

Correspondence and requests for materials should be addressed to Nicholas M. I. Taylor.

Peer review information *Nature Communications* thanks Denzel Eggermont and the other anonymous reviewer(s) for their contribution to the peer review of this work. A peer review file is available.